



The effect of Sr doping on structural and dielectric properties of Ba₂Co₂Fe₁₂O₂₂ ceramics

Q. S. Fu¹ · X. H. Chen¹ · C. Chakrabarti¹ · C. L. Li² · J. Zheng¹ · Y. H. Li¹ · Y. Qiu² · B. Meng¹ · S. L. Yuan¹

Received: 20 July 2019 / Accepted: 30 October 2019 / Published online: 9 November 2019
© Springer Science+Business Media, LLC, part of Springer Nature 2019

Abstract

Polycrystalline Ba_{2-x}Sr_xCo₂Fe₁₂O₂₂ (0 ≤ x ≤ 0.5) ceramics have been synthesized by the conventional solid-state-reaction method. From the analysis of X-ray diffraction and scanning electron microscopy, it can be obtained that the lattice parameters decrease monotonically with the increase in Sr doping content, while the average grain size presents a complicated trend. The dielectric measurements show that dielectric constants of all samples are larger than 10³ over a wide range of temperature and frequency (300–650 K and 1 kHz–1 MHz), which is identified as colossal dielectric constant. However, with the rise in Sr doping content, disparate evolutions of dielectric constant are found at 300 K and 600 K. A detailed study of dielectric response, impedance spectra and conductivity analysis suggest that the variation of dielectric constant at 300 K is dominated by the activation energy of relaxation, while that at 600 K is mainly in connection with the average grain size.

1 Introduction

The hexaferrites have been widely studied for several decades because of the practical and potential applications in permanent magnets, magnetic recording media, high frequency electromagnetic wave absorbers and stealth technologies [1–10]. Particularly, Y-type hexaferrites, which correspond to nominal compositions of Ba₂Me₂Fe₁₂O₂₂ (Me = Mg, Co, Zn, etc.), were found to be multiferroic materials with magnetoelectric coupling [11–18]. The molecular unit of Y-type hexaferrites is constructed by one S and one T block. The S block (with a unit formula Me₂Fe₄O₈) is formed by two spinel units and the T block (Ba₂Fe₈O₁₄) is made of four oxygen layers, in which Fe ions occupy both tetrahedral and octahedral sites while Ba²⁺ always replace O²⁻ ions somewhere in the oxygen lattice [2, 19, 20]. The special spiral magnetic structure of Y-type hexaferrites make

the presence of ferroelectric polarization induced by applied magnetic field.

Ba₂Co₂Fe₁₂O₂₂ is the first discovered ferroplana ferrite with an easy plane of magnetization perpendicular to the *c*-axis and exhibits attractive magnetic and dielectric properties [2, 16, 21]. Recently, in Sr-doped Y-type hexaferrites, the ferroelectric polarization induced by magnetic field could be observed at higher temperatures compared with undoped samples [11, 12, 22–25]. In addition, the dielectric properties are highly important for the application of multiferroic materials, especially for the microminiaturization of the electric devices [26, 27]. However, there are only a few studies on the dielectric properties of Sr-doped hexaferrites so far. [28, 29]. Therefore, the understanding of Sr doping effect on the dielectric properties of hexaferrites is still lacking.

In this work, systematic studies on the structural and dielectric properties of Sr-doped Ba₂Co₂Fe₁₂O₂₂ ceramics are performed. The result shows that dielectric constant presents different variation tendencies at 300 K and 600 K with increasing Sr doping content. The dielectric relaxation mechanisms and Sr doping effect are analyzed from the measurements of dielectric constant and dielectric loss. Afterwards the high temperature features are discussed based on the measurements and fits of impedance spectra and conductivity.

Q. S. Fu and X. H. Chen have contributed equally to this work.

✉ S. L. Yuan
yuansl@hust.edu.cn

¹ School of Physics, Huazhong University of Science and Technology, Wuhan 430074, People's Republic of China

² School of Physics and Electronic Engineering, Xinyang Normal University, Xinyang 464000, People's Republic of China

2 Experimental procedure

Polycrystalline ceramic samples of $\text{Ba}_{2-x}\text{Sr}_x\text{Co}_2\text{Fe}_{12}\text{O}_{22}$ ($0 \leq x \leq 0.5$) were prepared by the conventional solid-state-reaction method. Stoichiometric amount of high purity (99.99 %) BaCO_3 , SrCO_3 , Co_3O_4 , and Fe_2O_3 were weighed and mixed thoroughly in an agate mortar. The mixture was first calcined at 1373 K in air for 4 h. Then the resultant powders were adequately reground and pressed into pellets. Finally, the pellets were sintered in air at 1473 K for 18 h followed by slowly cooling down to room temperature at a rate of 1 K/min.

The crystal structures and microstructure of the ceramic samples were investigated by X-ray powder diffraction (XRD, Cu K, PANalytical) and scanning electron microscope (SEM, FEI Nova Nano SEM 450). Dielectric properties were measured using a precision impedance analyzer (Wayne Kerr 6500B).

3 Results and discussions

Room temperature XRD patterns of $\text{Ba}_{2-x}\text{Sr}_x\text{Co}_2\text{Fe}_{12}\text{O}_{22}$ ($0 \leq x \leq 0.5$) ceramics are refined using GSAS software based on a rhombohedral structure with $R\bar{3}m$ space group, as presented in Fig. 1a–e. The reliability factors (R_p , R_{wp} and χ^2) of the refinement are presented in corresponding figures. The small reliability factors are suggesting the high quality of refinements. The refined lattice parameters a , c and cell volume V are displayed in Fig. 1f. It is obvious that the lattice parameters and the cell volume decrease with the rise in Sr doping content, which is in accord with the smaller ionic radius of Sr^{2+} (1.32 Å) compared with that of Ba^{2+} (1.49 Å) [28].

SEM images and grain size distributions of $\text{Ba}_{2-x}\text{Sr}_x\text{Co}_2\text{Fe}_{12}\text{O}_{22}$ ceramics are given in Fig. 2a–j, respectively. It can be seen that the well-separated hexagonal plate like grains are presented for all samples. The grain size distribution was obtained from the corresponding SEM image by Nano Measurer software, from which the average grain size of each sample was calculated. Surprisingly, the average grain size shows a complicated trend with a maximum value of 3.57 μm for the $x=0.125$ sample and a minimum value of 2.56 μm for the $x=0.375$ sample (see Fig. 2k). With a little Sr doping content ($0 < x \leq 0.125$), Sr^{2+} might increase the growth rate of the ceramic sample. When $0.125 < x \leq 0.375$, the Sr^{2+} ions would reduce the stability of the bonds between the boundaries, leading to the reduction of the grain size [29]. With further rise in the doping content, the grain size increases again, which might be due to reduction of the activation energy of nucleation in the grains [30, 31].

In order to investigate the Sr doping effect on the dielectric properties of $\text{Ba}_2\text{Co}_2\text{Fe}_{12}\text{O}_{22}$ ceramics, the measurement of dielectric constant (ϵ') was performed in a frequency range from 100 Hz to 2 MHz at temperatures of 300 K and 600 K. Figure 3 shows the dielectric constant as a function of Sr doping content. At 300 K, ϵ' slightly increases with doping content x , reaches the maximum near $x=0.25$ and then monotonically decreases on further increase in x (see Fig. 3a). However, at 600 K, after a drop at $x=0.125$, ϵ' recovers until $x=0.375$ and then falls again at $x=0.5$ (see Fig. 3b). It should be noticed that the dielectric constants of all samples are higher than 10^3 at both 300 K and 600 K for each selected frequency, which can be called colossal dielectric constant [32, 33]. In addition, at both of the temperatures, ϵ' distinctly decreases with increasing frequency, which is due to the fact that the electron exchange cannot follow the variation of the applied electric field.

The dielectric response in $\text{Ba}_2\text{Co}_2\text{Fe}_{12}\text{O}_{22}$ is usually interpreted by the Maxwell–Wagner model [34, 35], where well conducting grains are separated by poorly conductive grain boundaries. The polarization effects can be categorized as intragranular and intergranular effects. The intragranular effect is in connection with the electron hopping between Fe^{2+} and Fe^{3+} as well as the hole transfer between Co^{2+} and Co^{3+} over the oxygen octahedrons within the grains, while the intergranular effect is related to the hopping of carriers between adjacent grains [15, 36]. For Sr doped samples, no extra carrier is introduced, hence the dielectric properties of doped samples have same origin as the undoped sample.

To further understand the Sr-doping effect on $\text{Ba}_2\text{Co}_2\text{Fe}_{12}\text{O}_{22}$, both dielectric constant and dielectric loss ($\tan\delta$) were measured with rising temperature under various frequencies. The experimental curves measured in the $x=0$ and 0.5 samples are illustrated in Fig. 4a, b as well as in the corresponding insets. As seen in the figures, the dielectric response at 1 kHz shows different temperature dependent behaviors in low and high temperature ranges. In the low-temperature range, ϵ' quickly increases with temperature, while it displays an almost temperature independent behavior in the high temperature range. The temperature region, in which ϵ' quickly increases, gradually shifts toward a higher temperature range with increasing frequency. Besides, the samples present colossal dielectric constant over a wide range of both temperature and frequency (300–650 K and 1 kHz–1 MHz). As seen in the insets of Fig. 4a, b, with the rise in the measuring temperature, the dielectric loss first rapidly increases, then displays a peak at temperature near which ϵ' shows a quick increase, and finally quickly increases again. To eliminate the influence of electrodes, the complex electric modulus (M^*) was defined as.

$$M^* = M' - iM'' = \frac{1}{\epsilon^*(\omega)}, \quad (1)$$

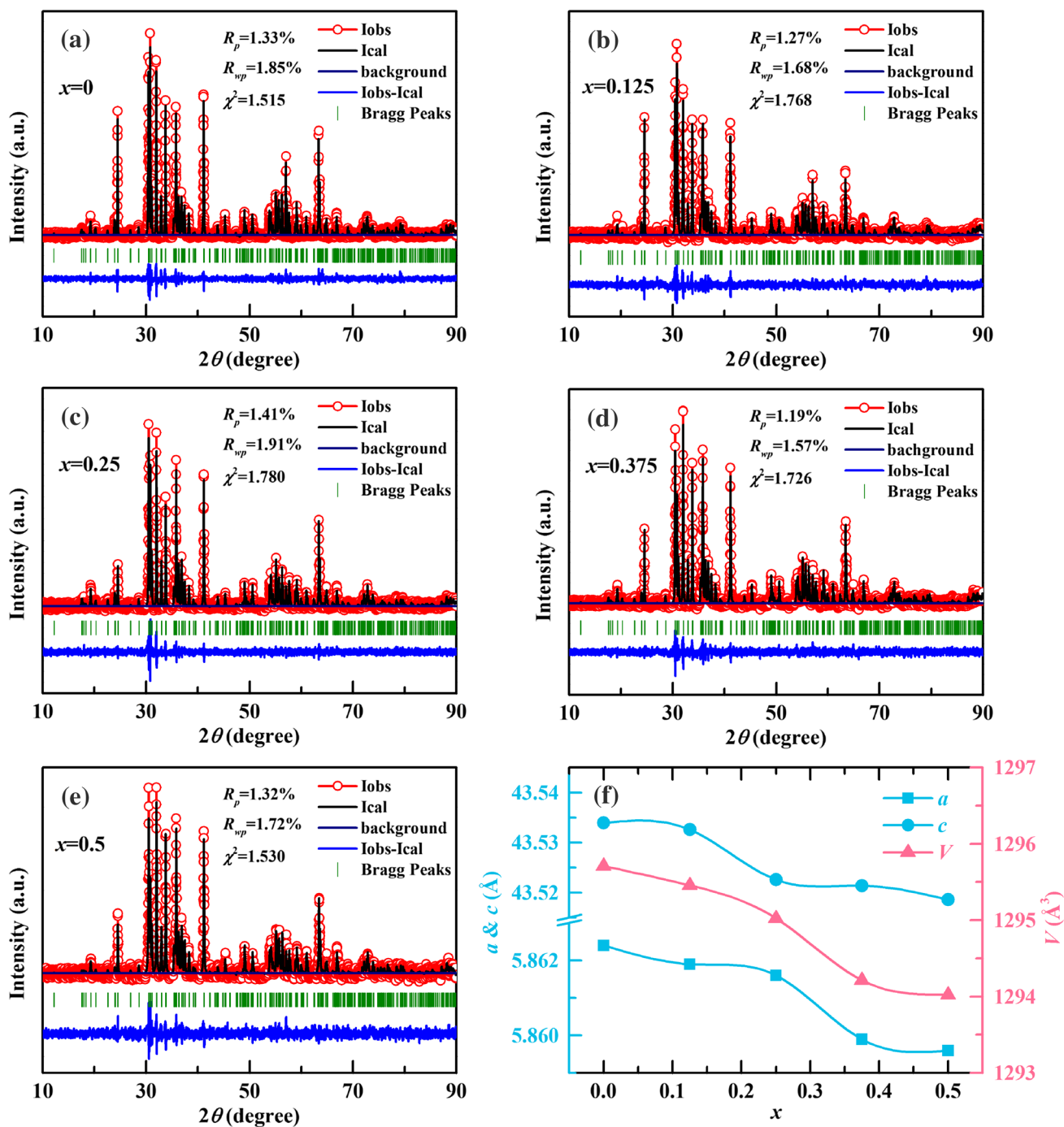


Fig. 1 a–e Room temperature XRD and refinement results of $Ba_{2-x}Sr_xCo_2Fe_{12}O_{22}$ ($0 \leq x \leq 0.5$). f The refined lattice parameter a , c and cell volume V as a function of Sr concentration

where M' and M'' are the real and imaginary parts of the complex electric modulus, respectively, and $\omega = 2\pi f$ is the angular frequency [37, 38]. The information of dielectric relaxation could be obtained from the peaks in $M''(T)$. M'' for the $x = 0$ and 0.5 samples are presented as a function of temperature, as seen in Fig. 4c, d. It is obvious that the peaks gradually shift toward higher temperature and the peak

intensity increases with a growth in frequency, indicating a thermally activate relaxation. The dielectric relaxation could be investigated based on the Arrhenius law:

$$f = f_0 \exp(-E_a / k_B T), \tag{2}$$

where f_0 is the pre-exponential factor, E_a is activation energy of the relaxation, and k_B is the Boltzmann constant [38, 39].

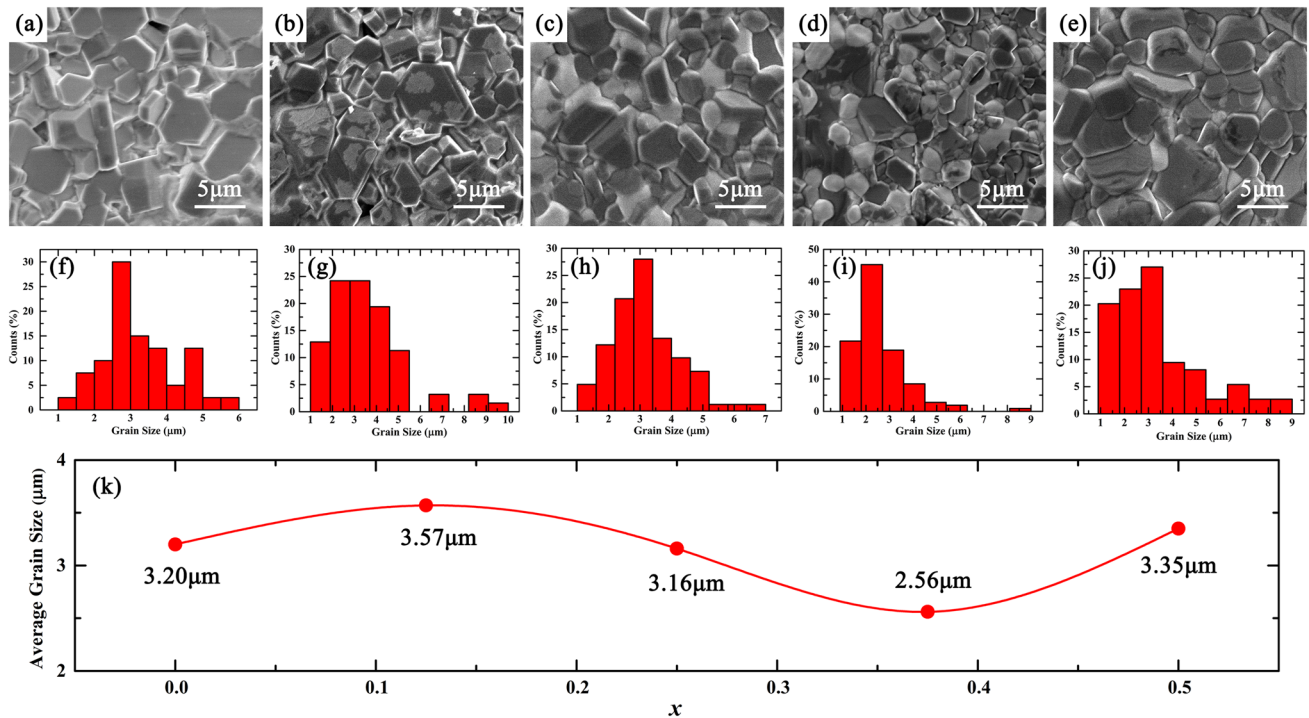


Fig. 2 SEM images and corresponding grain size distributions of $\text{Ba}_{2-x}\text{Sr}_x\text{Co}_2\text{Fe}_{12}\text{O}_{22}$ samples with (a, f) $x=0$, (b, g) $x=0.125$, (c, h) $x=0.25$, (d, i) $x=0.375$ and (e, j) $x=0.5$. (k) The average grain size as a function of Sr doping content x

The Arrhenius plots for the samples are illustrated in Fig. 4e. The activation energy is estimated from the slope of the linear fitting as presented in Fig. 4f. It can be seen that the activation energy first increases from 0.669 eV at $x=0$ to 0.688 eV at $x=0.25$, and then monotonically decreases to 0.651 eV at $x=0.5$. With the rise in the doping content, the variation tendency of the activation energy is in accordance with that of the dielectric constant at 300 K (see Fig. 3a), suggesting that, at a relatively lower temperature, Sr doping at Ba site could affect the activation energy and sequentially change the dielectric constant.

As mentioned above, the polarization originates from the contribution of grains and grain boundaries. It has been widely deemed that the polarization would be dominated by the intergranular effect at high temperature [39, 40]. For the purpose of identifying the effect of Sr doping on the polarization contributed from grains and grain boundaries, the impedance spectra of all samples were measured. The experimental data obtained at 450 K are plotted in the form of Z' vs. Z'' , in which two semicircular arcs were clearly observed, as shown in Fig. 5a–e. As reported in previous studies, low frequency (right sides) and high frequency arcs (left sides) are related to intergranular and intragranular relaxation, respectively [38–40]. The impedance data are further analyzed by the equivalent circuit shown in the inset of Fig. 5f, where R_{gb} and R_{g} represent the resistances of grain boundaries and

grains, respectively, $CPE1$ and $CPE2$ are constant phase elements. Based on such an equivalent circuit, R_{gb} and R_{g} are obtained and plotted as functions of Sr doping content in Fig. 5f. Clearly, with increasing Sr doping content, R_{g} monotonically increases, while R_{gb} shows a trend similar to the dielectric constant at 600 K (see Fig. 3b). Considering that the polarization of the samples at high temperature mainly comes from the space charges at the grain boundaries, the evolution of dielectric constant at high temperature with increasing Sr doping content might on account of the variation of R_{gb} .

To support the impedance results, ac conductivity analysis is conducted. Figure 6a–e show the ac conductivity as a function of frequency recorded at 450 K for $\text{Ba}_{2-x}\text{Sr}_x\text{Co}_2\text{Fe}_{12}\text{O}_{22}$ ($0 \leq x \leq 0.5$). It can be seen that all of the curves present a flat at low frequencies followed by a significant increase, and then a soft increase at high frequencies. According to previous studies [41, 42], the flat at low frequencies is connected with the jumping relaxation, since the frequency is exceedingly low and the electric field cannot upset the hopping conduction mechanism. Therefore, the flat value indicates the dc conductivity of the grain boundaries, which could be obtained directly from the conductivity plots. The significant increase and soft increase in the $\sigma(f)$ curves are due to the grain boundary blocking effect and the bulk conductivity relaxation, respectively [43]. In high frequency range, the ac

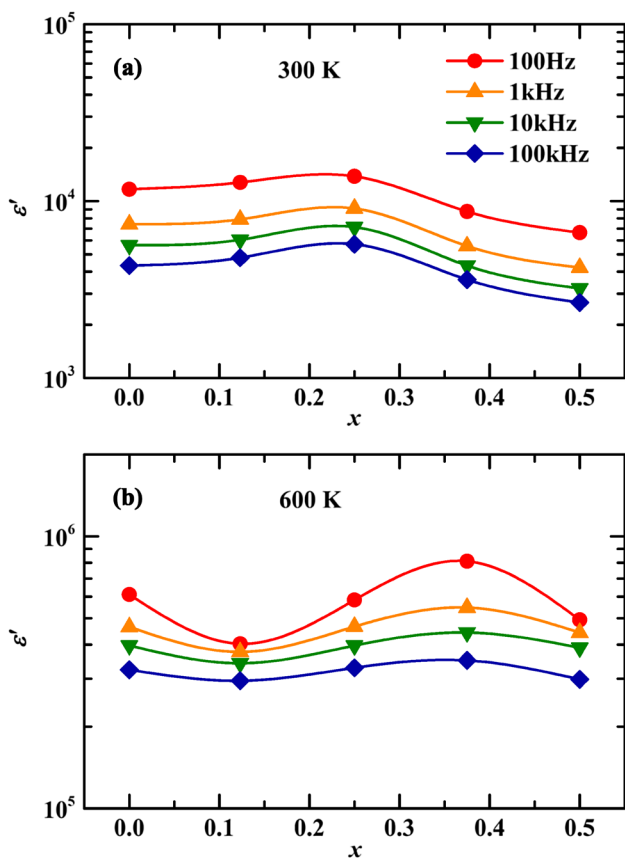


Fig. 3 Dielectric constant as a function of Sr doping content at **a** 300 K and **b** 600 K for selected frequencies of 100, 1 k, 10 k and 100 k Hz

conductivity could be described by “universal dielectric response” [44]:

$$\sigma = \sigma_g + a_0 f^s \tag{3}$$

where σ_g is the dc conductivity of grains, a_0 and s ($0 \leq s \leq 1$) are the temperature dependent constants. The lines at high frequencies are fitting curves based on Eq. (3). Moreover, the resistances of grain boundaries and grains can be calculated by $R_i = d/(\sigma_i S)$ ($i = gb$ or g), where d is the thickness of the sample and S is the area of the electrode, as presented in Fig. 6f. It is obvious that the variation tendency of R_{gb} and

R_g is consistent with the results from impedance analysis in Fig. 5f.

As indicated earlier, with the rise in the Sr doping content, the lattice parameters decreases and the crystal structure becomes more compact, leading to a reduction in the mobility of charge carriers and resulting in the increase of R_g [45, 46]. It should be noticed that R_{gb} (see Figs. 5f and 6f) shows the opposite trend to the average grain size (see Fig. 2k) with increasing Sr concentration. As the grain size decreases, more pores could be observed at the grain boundary region, which in turn increase the resistivity of grain boundaries, and hence hinder the hopping of charge carriers between adjacent grains. Meanwhile, this also causes an accumulation of space charges therein, which is beneficial to the enhancement of dielectric constant [47]. Based on the above results, the variation of dielectric constant at 600 K (see Fig. 3b) mainly originates from the impact of Sr doping on average grain size.

4 Conclusions

In this work, the structural and dielectric properties of Sr-doped $Ba_2Co_2Fe_{12}O_{22}$ ceramic samples have been investigated. The lattice parameters monotonically decrease while the average grain size shows a complicated trend with increasing Sr concentration. The dielectric measurements show that, with the rise in Sr doping content, the variations of dielectric constant present different tendencies at 300 K and 600 K. The evolution of dielectric constant at 300 K is suggested to be dominated by activation energy of the relaxation. The resistances of grain boundaries and grains, which are respectively in connection with the average grain size and the lattice parameters, are obtained from both the impedance spectra and conductivity analysis. Since intergranular effect would dominate at high temperature, the variation of dielectric constant at 600 K is mainly related to the average grain size.

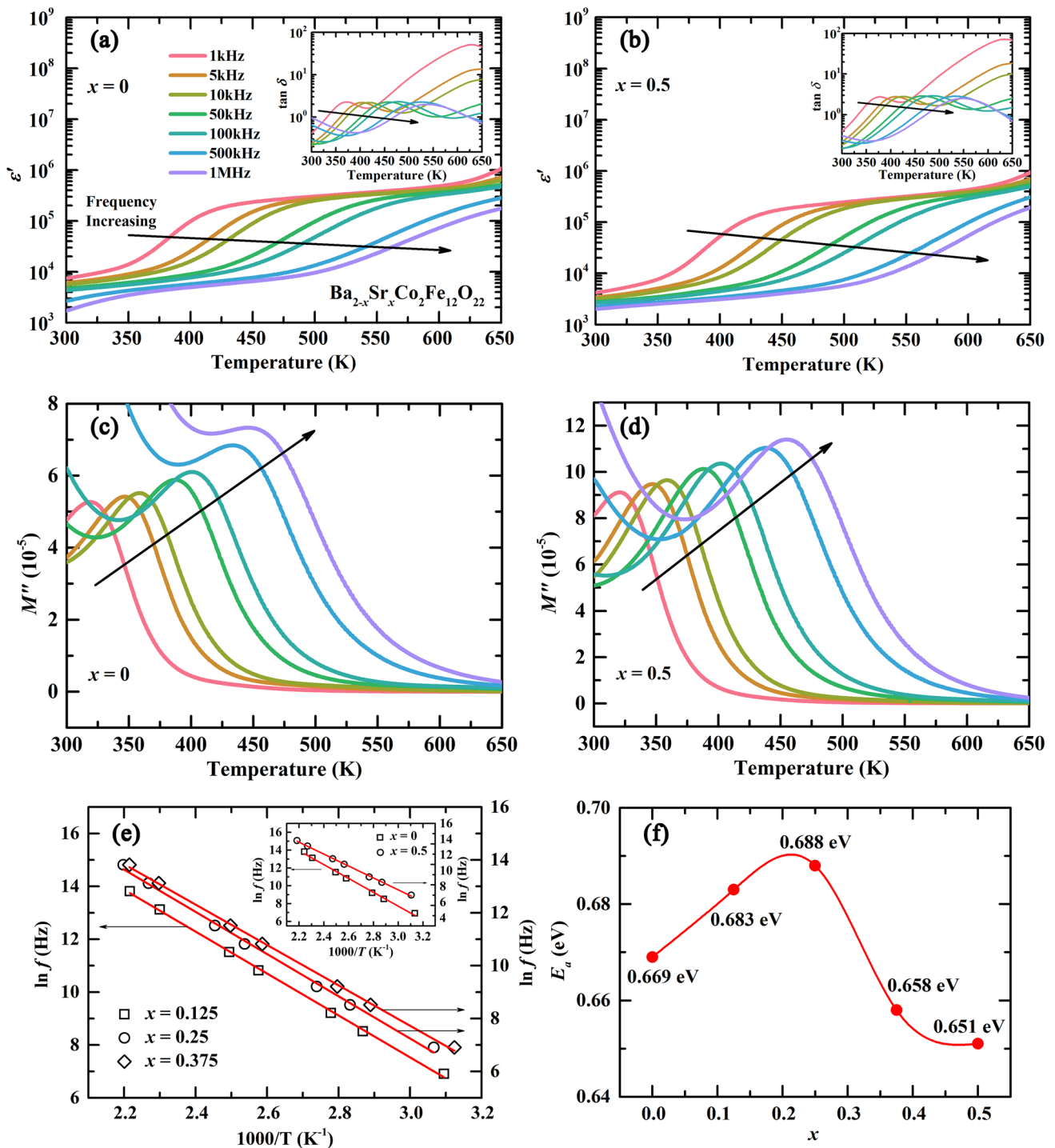


Fig. 4 Temperature dependence of dielectric response under different frequencies in the $x=0$ and 0.5 samples: dielectric constant (a, b), dielectric loss (the insets of a, b), imaginary of the complex elec-

tric modulus (c, d). e Arrhenius plots of the samples. f The activation energy as a function of doping content

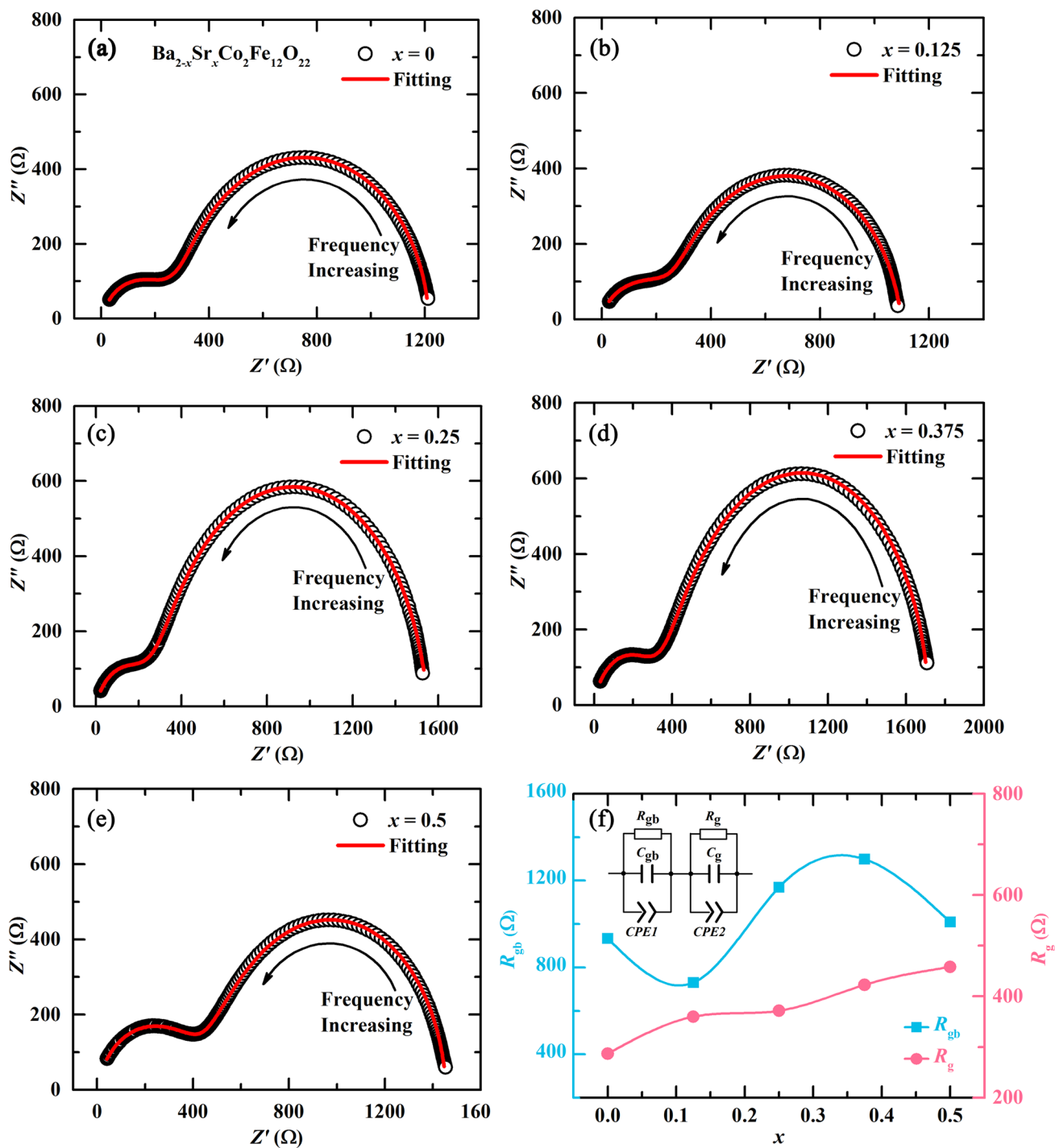


Fig. 5 a–e Nyquist plots of experimental data of impedance spectra measured at 450 K for samples of $x=0-0.5$. f Resistances of grain boundaries and grains as a function of doping content. The inset is the equivalent circuit

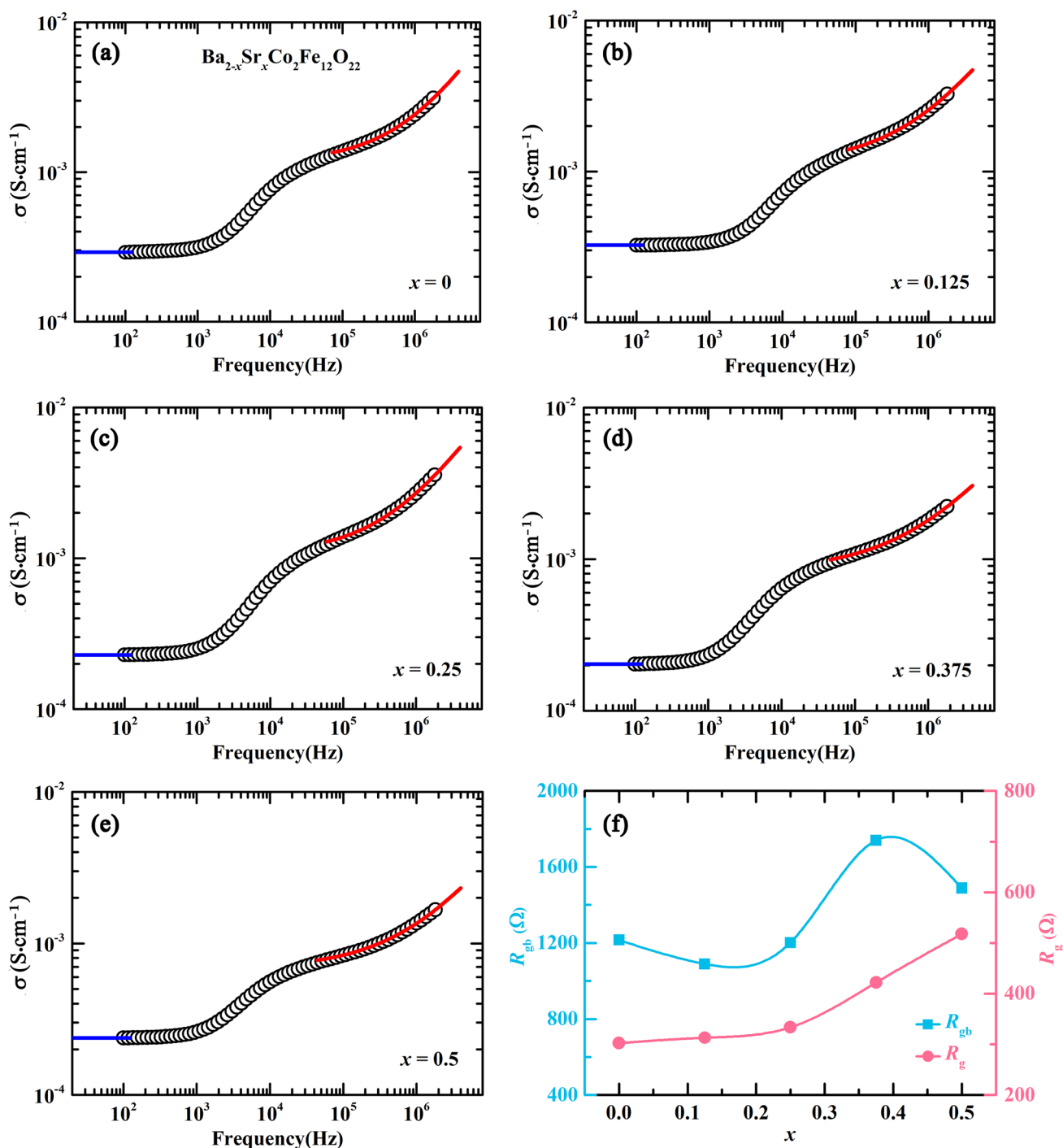


Fig. 6 a–e The frequency dependence of ac conductivity at 450 K for samples of $x=0$ – 0.5 . The lines at high frequencies (right sides) are fitting results based on Eq. (3), and the lines at low frequencies (left

sides) represent the dc conductivity of the grain boundaries. **f** Resistances of grain boundaries and grains as a function of doping content

Acknowledgements This work was supported by the National Natural Science Foundation of China (Grant Nos. 11474111 and 11604281) and Nanhu Scholars Program of XYNU. We would like to thank the staff of the Analysis Center of Huazhong University of Science and Technology for their assistance in various measurements.

References

1. K. Zhai, D.S. Shang, Y.S. Chai, G. Li, J.W. Cai, B.G. Shen, Y. Sun, Room-temperature nonvolatile memory based on a single-phase multiferroic hexaferrite. *Adv. Funct. Mater.* **28**, 1705771 (2018)

2. R.C. Pullar, Hexagonal ferrites: a review of the synthesis, properties and applications of hexaferrite ceramics. *Prog. Mater. Sci.* **57**, 1191–1334 (2012)
3. S. Mahmood, F. Jaradat, A.-F. Lehlooh, A. Hammoudeh, Structural properties and hyperfine interactions in Co–Zn Y-type hexaferrites prepared by sol–gel method. *Ceram. Int.* **40**, 5231–5236 (2014)
4. I. Sadiq, I. Ali, E.V. Rebrov, S. Naseem, M.N. Ashiq, M. Rana, Influence of Nd-Co substitution on structural, electrical, and dielectric properties of x-type hexagonal nanoferrites. *J. Mater. Eng. Perform.* **23**, 622–627 (2014)
5. W. Eerenstein, N. Mathur, J.F. Scott, Multiferroic and magnetoelectric materials. *Nature* **442**, 759 (2006)
6. Y. Tokura, S. Seki, Multiferroics with spiral spin orders. *Adv. Mater.* **22**, 1554–1565 (2010)
7. M.J. Iqbal, R.A. Khan, Enhancement of electrical and dielectric properties of Cr doped BaZn₂ W-type hexaferrite for potential applications in high frequency devices. *J. Alloy. Compd.* **478**, 847–852 (2009)
8. M.N. Ashiq, M.J. Iqbal, I.H. Gul, Structural, magnetic and dielectric properties of Zr–Cd substituted strontium hexaferrite (SrFe₁₂O₁₉) nanoparticles. *J. Alloy. Compd.* **487**, 341–345 (2009)
9. M. Soda, T. Ishikura, H. Nakamura, Y. Wakabayashi, T. Kimura, Magnetic ordering in relation to the room-temperature magnetoelectric effect of Sr₃Co₂Fe₂₄O₄₁. *Phys. Rev. Lett.* **106**, 087201 (2011)
10. C. Yuan, Y. Hong, Microwave adsorption of core–shell structure polyaniline/SrFe₁₂O₁₉ composites. *J. Mater. Sci.* **45**, 3470–3476 (2010)
11. Y. Wang, S. Zhang, W. Zhu, L. Ling, L. Zhang, Z. Qu, L. Pi, W. Tong, M. Tian, Y. Zhang, Nonzero electric polarization and four magnetoelectric states at zero magnetic field in Cr-doped Y-type hexaferrite. *Appl. Phys. Lett.* **110**, 262901 (2017)
12. J. Vít, F. Kadlec, C. Kadlec, F. Borodavka, Y.S. Chai, K. Zhai, Y. Sun, S. Kamba, Electromagnon in the Y-type hexaferrite BaSrCoZnFe₁₁AlO₂₂. *Phys. Rev. B* **97**, 134406 (2018)
13. K. Zhai, Y. Wu, S. Shen, W. Tian, H. Cao, Y. Chai, B.C. Chakoumakos, D. Shang, L. Yan, F. Wang, Giant magnetoelectric effects achieved by tuning spin cone symmetry in Y-type hexaferrites. *Nat. Commun.* **8**, 519 (2017)
14. G. Wang, S. Cao, Y. Cao, S. Hu, X. Wang, Z. Feng, B. Kang, Y. Chai, J. Zhang, W. Ren, Magnetic field controllable electric polarization in Y-type hexaferrite Ba_{0.5}Sr_{1.5}Co₂Fe₁₂O₂₂. *J. Appl. Phys.* **118**, 094102 (2015)
15. S. Hirose, K. Haruki, A. Ando, T. Kimura, Mutual control of magnetization and electrical polarization by electric and magnetic fields at room temperature in Y-type BaSrCo_{2-x}Zn_xFe₁₁AlO₂₂ ceramics. *Appl. Phys. Lett.* **104**, 022907 (2014)
16. M. Wu, W. Zhong, X. Gao, L. Liu, Z. Liu, Analysis of the alternating current conductivity and magnetic behaviors for the polycrystalline Y-type Ba_{0.5}Sr_{1.5}Co₂(Fe_{1-x}Al_x)₁₂O₂₂ hexaferrites. *J. Appl. Phys.* **116**, 224103 (2014)
17. T. Kimura, G. Lawes, A. Ramirez, Electric polarization rotation in a hexaferrite with long-wavelength magnetic structures. *Phys. Rev. Lett.* **94**, 137201 (2005)
18. R. Pullar, M.D. Taylor, A. Bhattacharya, Magnetic Co₂Y ferrite, Ba₂Co₂Fe₁₂O₂₂ fibres produced by a blow spun process. *J. Mater. Sci.* **32**, 365–368 (1997)
19. C. Sudakar, G. Subbanna, T. Kutty, Wet chemical synthesis of multicomponent hexaferrites by gel-to-crystallite conversion and their magnetic properties. *J. Magn. Magn. Mater.* **263**, 253–268 (2003)
20. A. Elahi, M. Ahmad, I. Ali, M. Rana, Preparation and properties of sol–gel synthesized Mg-substituted Ni₂Y hexagonal ferrites. *Ceram. Int.* **39**, 983–990 (2013)
21. P. Behera, S. Ravi, Magnetic and dielectric spectroscopic studies in Zn substituted Y-type barium hexaferrite. *J. Alloy. Compd.* **767**, 712–723 (2018)
22. S.H. Chun, Y.S. Chai, Y.S. Oh, D. Jaiswal-Nagar, S.Y. Haam, I. Kim, B. Lee, D.H. Nam, K.-T. Ko, J.-H. Park, Realization of giant magnetoelectricity in helimagnets. *Phys. Rev. Lett.* **104**, 037204 (2010)
23. H.B. Lee, S.H. Chun, K.W. Shin, B.-G. Jeon, Y.S. Chai, K.H. Kim, J. Schefer, H. Chang, S.-N. Yun, T.-Y. Joung, Helical magnetic order and field-induced multiferroicity of the Co₂ Y-type hexaferrite Ba_{0.3}Sr_{1.7}Co₂Fe₁₂O₂₂. *Phys. Rev. B* **86**, 094435 (2012)
24. Y. Hiraoka, H. Nakamura, M. Soda, Y. Wakabayashi, T. Kimura, Magnetic and magnetoelectric properties of Ba_{2-x}Sr_xNi₂Fe₁₂O₂₂ single crystals with Y-type hexaferrite structure. *J. Appl. Phys.* **110**, 033920 (2011)
25. S. Hirose, K. Haruki, A. Ando, T. Kimura, Effect of high-pressure oxygen annealing on electrical and magnetoelectric properties of BaSrCo₂Fe₁₁AlO₂₂ ceramics. *J. Am. Ceram. Soc.* **98**, 2104–2111 (2015)
26. Z. Kutnjak, J. Petzelt, R. Blinc, The giant electromechanical response in ferroelectric relaxors as a critical phenomenon. *Nature* **441**, 956 (2006)
27. X. Zeng, J. Sun, Y. Yao, R. Sun, J.B. Xu, C.P. Wong, A combination of boron nitride nanotubes and cellulose nanofibers for the preparation of a nanocomposite with high thermal conductivity. *ACS Nano* **11**, 5167–5178 (2017)
28. H. Khanduri, M. Chandra Dimri, H. Kooskora, I. Heinmaa, G. Viola, H. Ning, M. Reece, J. Krustok, R. Stern, Structural, dielectric, magnetic, and nuclear magnetic resonance studies of multiferroic Y-type hexaferrites. *J. Appl. Phys.* **112**, 073903 (2012)
29. L. Zhang, W. Zhong, C. Wang, P. Zhang, Y. Wang, Finite-size effects in ferroelectric solid solution Ba_xSr_{1-x}TiO₃. *J. Phys. D* **32**, 546–551 (1999)
30. K.R. Obulesu, T.S. Rao, K.J. Raju, Magnetic and microwave dielectric properties of Y-type Sr doped Ba₂Zn₂Fe₁₂O₂₂ hexagonal ferrite. *J. Alloy. Compd.* **695**, 3030–3035 (2017)
31. W. Xu, J. Yang, W. Bai, Y. Zhang, K. Tang, C. Duan, X. Tang, J. Chu, Effects of aluminum substitution on the crystal structure and magnetic properties in Zn₂Y-type hexaferrites. *J. Appl. Phys.* **117**, 17D909 (2015)
32. P. Lunkenheimer, V. Bobnar, A.V. Pronin, A. Ritus, A. Volkov, A. Loidl, Origin of apparent colossal dielectric constants. *Phys. Rev. B* **66**, 052105 (2002)
33. C. Li, S. Huang, X. Chen, T. Yan, Q. Fu, R. Zhang, C. Zhu, S. Yuan, Colossal dielectric response and relaxation properties in Co₂Z-type hexaferrites. *Ceram. Int.* **43**, 12435–12441 (2017)
34. A. Abo El Ata, M. El Hiti, M. El Nimr, Room temperature electric and dielectric properties of polycrystalline BaCo_{2-x}Zn_xFe_{12-2x}O₁₉. *J. Mater. Sci. Lett.* **17**, 409–413 (1998)
35. M. Costa, G. Pires Jr., A. Terezo, M. Graca, A. Sombra, Impedance and modulus studies of magnetic ceramic oxide Ba₂Co₂Fe₁₂O₂₂ (Co₂Y) doped with Bi₂O₃. *J. Appl. Phys.* **110**, 034107 (2011)
36. V. Murthy, J. Sobhanadri, Dielectric properties of some nickel-zinc ferrites at radio frequency. *Phys. Status Solidi A* **36**, K133–K135 (1976)
37. K. Wang, C. Wang, Aluminum-vacancy-related dielectric relaxations in AlN ceramics. *J. Am. Ceram. Soc.* **101**, 2009–2016 (2018)
38. L. Tong, H. Li, W. Ni, Y. Guo, Q. Li, H. Wang, C. Wang, High-temperature colossal dielectric behavior of BaZrO₃ ceramics. *RSC Adv.* **7**, 33708–33713 (2017)

39. R. Tang, C. Jiang, J. Jian, Y. Liang, X. Zhang, H. Wang, H. Yang, Impedance spectroscopy and scaling behaviors of $\text{Sr}_3\text{Co}_2\text{Fe}_{24}\text{O}_{41}$ hexaferrite. *Appl. Phys. Lett.* **106**, 022902 (2015)
40. C. Li, T. Yan, G. Barasa, Y. Li, R. Zhang, S. Huang, S. Yuan, Colossal dielectric response in $\text{Ba}_{1.5}\text{Sr}_{1.5}\text{Co}_2\text{Fe}_{24}\text{O}_{41}$ ceramics at high-temperature. *J. Mater. Sci.* **29**, 9971–9978 (2018)
41. L. Liu, C. Wang, X. Sun, G. Wang, C. Lei, T. Li, Oxygen-vacancy-related relaxations of $\text{Sr}_3\text{CuNb}_2\text{O}_9$ at high temperatures. *J. Alloy. Compd.* **552**, 279–282 (2013)
42. W. Li, R.W. Schwartz, ac conductivity relaxation processes in $\text{CaCu}_3\text{Ti}_4\text{O}_{12}$ ceramics: grain boundary and domain boundary effects. *Appl. Phys. Lett.* **89**, 242906 (2006)
43. L. Zhang, Z.J. Tang, Polaron relaxation and variable-range-hopping conductivity in the giant-dielectric-constant material $\text{CaCu}_3\text{Ti}_4\text{O}_{12}$. *Phys. Rev. B* **70**, 174306 (2004)
44. S. Elliott, Ac conduction in amorphous chalcogenide and pnictide semiconductors. *Adv. Phys.* **36**, 135–217 (1987)
45. Ashima, S. Sanghi, A. Agarwal, Reetu, N. Ahlawat, Monica, Structure refinement and dielectric relaxation of M-type Ba, Sr, Ba-Sr, and Ba-Pb hexaferrites. *J. Appl. Phys.* **112**, 14–110 (2012)
46. M.J. Iqbal, M.N. Ashiq, I.H. Gul, Physical, electrical and dielectric properties of Ca-substituted strontium hexaferrite ($\text{SrFe}_{12}\text{O}_{19}$) nanoparticles synthesized by co-precipitation method. *J. Magn. Mater.* **322**, 1720–1726 (2010)
47. H.-I. Hsiang, F.-S. Yen, Y.-H. Chang, Effects of doping with La and Mn on the crystallite growth and phase transition of BaTiO_3 powders. *J. Mater. Sci.* **31**, 2417–2424 (1996)

Publisher's Note Springer Nature remains neutral with regard to jurisdictional claims in published maps and institutional affiliations.